Mechanical Systems and Signal Processing 132 (2019) 232–252

Contents lists available at ScienceDirect

Mechanical Systems and Signal Processing

journal homepage: www.elsevier.com/locate/ymssp

Spring amplification and dynamic friction modelling of a 2DOF/2SDOF system in an electromagnetic vibration energy harvester – Experiment, simulation, and analytical analysis

Chung Ket Thein [a,*], Faruq Muhammad Foong [a], Yi-Chung Shu [b]

[a] *School of Engineering and Physical Sciences, Heriot-Watt University, No. 1, Jalan Venna P5/2, Precinct 5, 62200, Malaysia*
[b] *Institute of Applied Mechanics, National Taiwan University, Taipei 106, Taiwan, Republic of China*

ARTICLE INFO

Article history:
Received 10 January 2019
Received in revised form 1 June 2019
Accepted 20 June 2019

Keywords:
Electromagnetic vibration energy harvesting
Spring
2DOF and 2SDOF
Dynamic friction
Power density

ABSTRACT

A cantilever beam-based vibration energy harvester is generally preferred due to its simplicity and effectiveness as compared to a spring mass system. This paper analyses the use of a spring to amplify the performance of a conventional single degree of freedom (SDOF) cantilever beam-based vibration energy harvester. A spring was introduced to modify the conventional SDOF design into a two single degree of freedom (2SDOF) system and a two degree of freedom (2DOF) system. The motion of the spring was restricted in the vertical motion using a slider and a linear guide rail fixed to the vibrating base, hence introducing a dynamic friction into the system. Both designs were analysed under three different cases to observe the effect of natural frequency reduction on the frequency bandwidth and power harvested by each design. The vibration-friction interaction in the designs was modelled based on the concept of relative motion. Two different friction theories were applied and verified with simulation and experiment. It was shown that the stick condition would not occur in a SDOF system with a dynamic friction interaction. It was also found that it is possible to tune the friction force of a dynamic friction surface to induce a favourable output at the isolation frequencies of a 2DOF system. Analysis shows that the 2DOF design displayed a larger power density than the conventional SDOF design below a certain natural frequency value, being 78.1% higher at 9.5 Hz. The power densities of the 2SDOF design were almost similar to the SDOF design. However, the 2SDOF design displayed a significant drop in power when under the condition of matched natural frequencies. Nevertheless, the frequency bandwidth of the 2SDOF design can be improved by tuning its two resonant peaks closer to each other.

1. Introduction

The concept of generating power from mechanical vibrations to sustain low powered devices was introduced approximately two decades ago [1]. Since then, research in vibration energy harvesting area have grown due to its promising capabilities [2–4]. The two most common single degree of freedom (SDOF) harvester configuration is by having a mass suspended on a spring or a clamp-free cantilever beam clamped to a vibrating base. However, the latter is proven to be more popular due to its simplicity. In addition, Erturk and Inman [5] showed that the output amplitude of a cantilever beam can reach up

* Corresponding author.
E-mail address: ckthein@gmail.com (C.K. Thein).

https://doi.org/10.1016/j.ymssp.2019.06.028
0888-3270/

to 56.6% higher than a spring mass system for the same damping and base excitation input. However, using a spring can significantly reduce the overall volume of the harvester as compared to using a beam.

Past research have explored the possibilities of different spring mass like systems or cantilever based designs in an attempt to increase the power output and frequency bandwidth of a vibration energy harvester. Some researchers have used the repulsive effect of alike pole magnets to act as springs [6–10]. This arrangement resulted in a bi-stable systems in where the frequency bandwidth was reported to significantly increase. Ooi and Gilbert studied the use of a dual cantilever beam system in electromagnetic vibration energy harvester application [11]. It was shown that due to the difference in phase angle between the coil and the magnets, the bandwidth of the system can be increase. Foong et al. suggested a similar concept with the focus on anti-phase resonance to increase the relative velocity between the coil and the magnets and hence significantly increase its power output [12]. Wong et al. proposed a multi degree of freedom system to increases the number of resonant peaks and power output of an electrostatic vibration energy harvester based on the concept of superposition [13]. Similarly, Liu et al. applied the same concept by using an array of clamp free cantilever beams to increase the bandwidth of a piezoelectric harvester [14–16]. Nevertheless, not many works has been conducted in the use of an actual spring in vibration energy harvester applications. Depending on design and application, using a spring has the potential to reduce the volume of a harvester as compared to a beam.

In theory, the vibration of a mass on a helical spring is assumed to move in only one direction. This would not be the case in practical applications as depending on the weight of the mass and the stiffness of the spring, the spring can be subjected to buckling in where the spring bends in the lateral direction. The buckling effect can be suppressed by either vibrating the mass horizontally on a flat surface or by attaching some sort of guide system to ensure that the mass only vibrates in the desired direction. However, both cases would inevitably introduce friction into the system. Friction in a vibrating system is often described as a non-linear phenomena due to its complex interaction. In some cases, non-linear vibration behaviour is desirable as it was shown to improve the performance of a harvester [17]. One of the most common method used to model this friction is the Coulomb friction model [18–20]. Several mathematical models have been well established in past literatures, considering cases of a static friction surface [21,22] or a friction surface travelling under constant velocity [23,24]. However, a friction model for the case of a dynamic vibrating friction surface have yet to be demonstrated.

This study explores the use of a spring to modify and amplify the performance of a conventional SDOF cantilever beam-based electromagnetic vibration energy harvester in terms of its power output, while maintaining the same overall volume. In addition, the effect of a dynamic surface friction on the performance of the harvester was also studied. For the first modification, a spring was attached to the magnets and fixed onto the vibrating base while the cantilever beam remain clamped to the vibrating base, creating two single degree of freedom (2SDOF) systems. The second modification was to apply the spring to the base of the cantilever beam instead while the magnets remained clamped to the vibrating base. This resulted in a two degree of freedom system (2DOF). A mechanical slider and a linear guiderail was used to ensure that the spring vibrates vertically. The mechanical slider was attached to the vibrating mass whereas the linear guiderail was fixed to the vibrating base. The mathematical models for a single degree of freedom (SDOF) spring mass and cantilever beam system as well as a two degree of freedom (2DOF) spring mass system were presented. In addition, the friction behaviour for a dynamic vibrating friction surface was also modelled to account for the friction between the slider and the guiderail. The theoretical equations were verified with experiment and finite element analysis (FEA) simulations for three different cases. The effect of friction on the performance of the 2SDOF and 2DOF design was thoroughly discussed. Lastly, the peak power output and power densities of all three designs were compared and analysed.

2. Basic theory

In this study, two different vibrations system will be studied, namely the 2DOF and the 2SDOF systems and compared to a conventional SDOF cantilever beam-based vibration energy harvester design represented by a clamp free beam. The overall volume of all harvesters were fixed. This section describes the basic theory and governing equations for a SDOF and 2DOF spring-mass system with viscous damping and a dynamic surface friction, a cantilever beam with tip mass and the power output of an electromagnetic energy harvester.

2.1. Mathematical model of SDOF and 2DOF spring-mass system under harmonic base excitation with viscous damping and surface friction

Consider the following simplified models for a SDOF and 2DOF spring-mass vibration system shown in Fig. 1. Here, m_p, k_p and c_p refers to the mass, spring stiffness and damping constant of each masses where $p = 0, 1$ and 2, corresponding to the masses in Fig. 1. x_p describes the absolute vertical motion of each mass under a sinusoidal base excitation input of $Ysin(\omega t)$. Finally, F_R refers to the magnitude of the frictional force between the mass and a frictional surface. The sign change for $F_R$will be explained in the next section.

Assuming the spring to be massless, the governing equation for the SDOF model at time t is

$$m_0\ddot{x}_0 + c_0\dot{x}_0 + k_0x_0 = k_0Ysin(\omega t) \mp F_R \tag{1}$$

whereas for the 2DOF system,

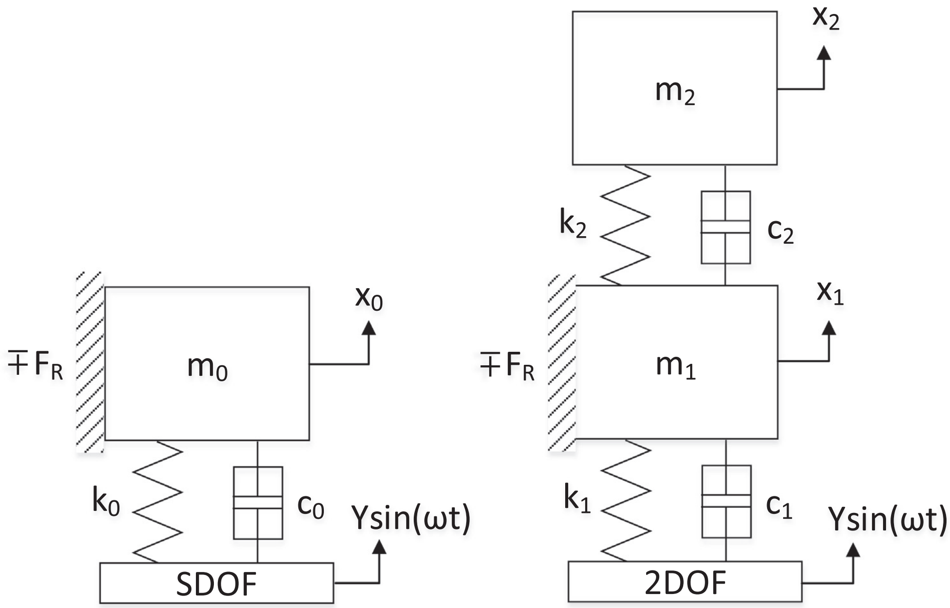

Fig. 1. Cantilever beam with a lumped mass placed on the free-end of the beam.

$$m_1\ddot{x}_1 + c_1\dot{x}_1 + k_1x_1 + c_2(\dot{x}_2 - \dot{x}_1) + k_2(x_1 - x_2) = k_1Ysin(\omega t) \mp F_R \tag{2}$$

$$m_2\ddot{x}_2 - c_2(\dot{x}_2 - \dot{x}_1) - k_2(x_1 - x_2) = 0 \tag{3}$$

$$Y = G/\omega^2 \tag{4}$$

$$F_R = \mu F_L \tag{5}$$

where Y and G are the amplitude and acceleration of the base excitation input, ω is the driving frequency of base, μ is the coefficient of friction between the two contact surfaces and F_L is the normal load acting on the contact surfaces. The second derivative represents the acceleration and the first derivative is the velocity. In most practical applications, masses are usually vibrated under a constant base acceleration. This will result in a change of the Y value at different frequencies. The damping constants in Eqs. (1)–(3) can be related to their corresponding damping ratios, ζ_p, as follow

$$\zeta_p = \frac{c_p}{2\sqrt{k_p m_p}} \tag{6}$$

Eqs. (1)–(3) can be solved by assuming the following steady-state solution

$$x_p(t) = B_p sin(\omega t) + D_p cos(\omega t) \tag{7}$$

The constants B_p and D_p can be determined by substituting Eq. (7) into Eqs. (2) and (3) and equating the sine and cosine terms. Applying the trigonometrical identities, Eq. (7) can be rewritten as

$$x_p(t) = A_p sin(\omega t + \theta_p) \tag{8}$$

$$A_p = \sqrt{{B_p}^2 + {D_p}^2} \tag{9}$$

$$\theta_p = tan^{-1}\left(\frac{D_p}{B_p}\right) \tag{10}$$

where A_p is defined as the absolute steady-state amplitude of the response and θ_p is the respective phase angle.

2.2. Theoretical friction modelling for a dynamic friction surface

Consider the case where m_0 and m_1 are the only masses in contact with the friction surface for the SDOF and 2DOF model, respectively. Normally the friction surface is usually modelled as a static surface [21,22]. In this case, the friction force direction will always oppose the motion of m_0 and m_1. However, if the friction surface was to vibrate together with the base, the friction surface would become a dynamic surface. The direction of the friction force is then strongly related to the relative velocity between the vibrating mass in contact and friction surface. For two sliding surfaces, the direction of friction force acting on one contact surface would not necessarily be the same as the other surface. For a vibrating mass, the steady-state velocity of the mass is simply the product of the steady-state amplitude and the vibrating frequency. However, since the mass in contact and the friction surface are vibrating under the same frequency, the friction direction can be directly related to the absolute steady-state amplitude of the mass in contact, A_p and the base amplitude, Y. Fig. 2 illustrates the direction of the friction force acting on the mass in contact for four different cases.

For cases (a) and (c), the magnitude of A_p is larger than Y. This means that the direction of the mass in contact relative to the friction surface would be equal to the direction of A_p. Hence, the direction of the friction force acting on the mass in contact is opposite to the direction of A_p. For cases (b) and (d), the magnitude of Y is larger than A_p. Therefore, the direction of the mass in contact relative to the friction surface would in the direction of Y, making the direction of the frictional force to be equal to the direction of A_p. Overall, the mass in contact would experience an opposing friction force ($-F_R$) when the magnitude of $A_p > Y$ and a contributing friction force ($+F_R$) when the magnitude of $A_p < Y$. This suggest that the direction of the friction force in highly dependent on the magnitude of Y and A_p and the phase angle of A_p, as the phase angle of A_p determines the direction of A_p. Fig. 3(a) describes the change in friction direction for a SDOF system and Fig. 3(b) illustrates the change in direction between the mass in contact and the friction surface with respect to the phase angle of the mass, θ_p.

Fig. 3(a) shows that the frequency at which the friction changes direction is located at the intersection between A_p and Y. This frequency is known as the isolation frequency, ω_I, in where it is defined as the point at where the output response changes from higher to lower than the input response or from lower to higher. Fig. 3(b) describes how the direction of A_p changes according to its phase angle. It shows that be for the resonance frequency, ω_n, the direction of A_p is aligned with the dynamic friction surface whereas after, ω_n, A_p vibrates in the opposite direction with respect to Y. One can note that Fig. 3(a) only display a single point of intersection between A_p and Y, which is expected for a SDOF system with a single vibration mode. However, a 2DOF system may experience two or more intersection frequencies depending on the significance of the second mode. For this case, the friction direction would be expected to change at each intersection.

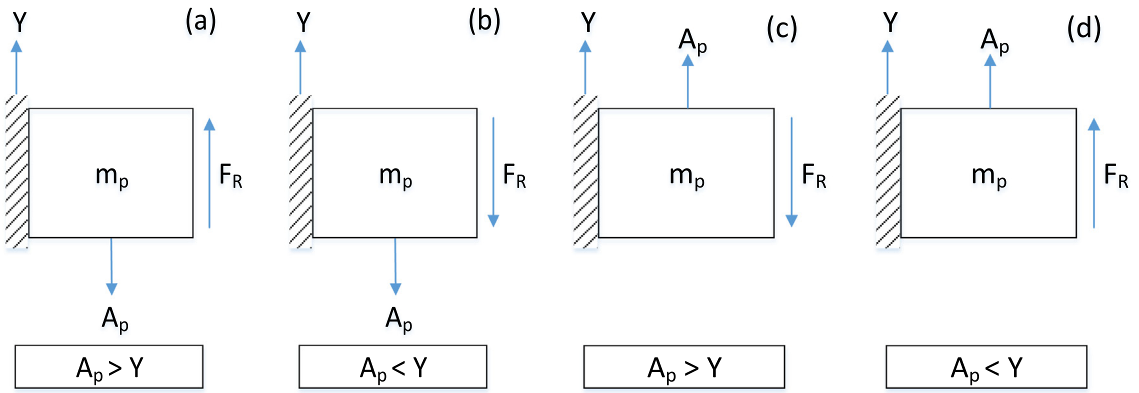

Fig. 2. Direction of friction force acting on the vibrating mass for four different scenarios.

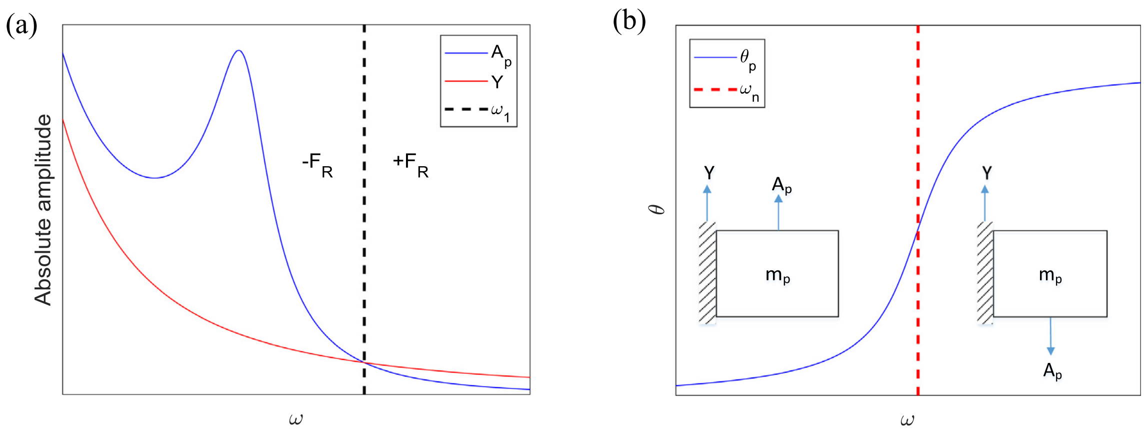

Fig. 3. (a) Change in friction direction of a SDOF system. (b) Change in motion direction of SDOF system.

It is important to understand that the first isolation frequency for a structure under linear base excitation vibration must be evaluated under the consideration of an opposing friction force ($-F_R$) acting on the mass in contact and not under frictionless condition. This is because friction is already present in the system and will affect the amplitude of A_p regardless of the base input. In addition, A_p will always be higher than Y before the first isolation frequency and would hence experience and opposing friction force. After the first isolation frequency, the mass in contact would experience a contributing friction force ($+F_R$). If a second isolation frequency exist, then it must be evaluated under consideration of $+F_R$.

A SDOF system would generally only have a single isolation frequency. However, a 2DOF system with a significant second mode may experience more. Therefore, every subsequent isolation frequency must be evaluated depending on the direction of the friction force. Fig. 4(a) and (b) explain the correct method in evaluating the isolations frequencies of a SDOF and a 2DOF system. The vertical axis in Fig. 4 was plotted using a log scale to aid visually. The black markers represent the isolation frequencies of the system.

In this paper, the change in friction force direction and magnitude was only considered at ω_I and was assumed to behave in two different manners. At other frequencies, the friction force magnitude is assumed to be equal to F_R. The first method (Theory 1) was to assume that the transition of the friction force direction and magnitude at ω_I behaves in a similar manner to the transition of the phase angle at each resonance mode. This theory is comparable to a modified Coulomb friction model. For each intersection point, this change can be estimated based on the following equations

$$F_R = \pm F_R\left(\frac{\theta}{\bar{a}} - 1\right) \tag{11}$$

$$\theta = tan^{-1}\left(\frac{2\omega\omega_I\zeta_p}{\omega_I{}^2 - \omega^2}\right) \tag{12}$$

where $\zeta_p = \zeta_0$ for the SDOF model and $\zeta_p = \zeta_1$ for the 2DOF model and $\bar{a}$ is the average value between the maximum and minimum value of θ. It is worth to mention that θ actually represents another form of the phase angle equation for a SDOF system. The sign change indicate how the friction direction changes, either from negative to positive ($+F_R$) or from positive to negative ($-F_R$). This assumption assumes that the magnitude and direction of the friction forces changes accordingly at the isolation frequencies. The rate of change is solely dependent on ζ_p. The second method (Theory 2) was to assume that the change in friction is abrupt, and changes suddenly from negative to positive at each isolation frequency. In this assumption, only the direction of the friction force changes at the isolation frequencies whereas the magnitude of the force is constant. This theory is similar to the classical Coulomb friction model in terms that the friction force magnitude is independent of the vibrating velocity [25]. Generally, the coulomb friction law is applied for dry friction cases.

Normally, for an object to move on a friction surface, the force exerted on the object must be larger than the frictional force acting on the object. Otherwise, the object would remain stuck to the friction surface. This phenomena is commonly known as the stick-slip phenomena. In general, the stick condition would occur when the resultant force between the force exerted on the mass and the friction force is smaller than zero and the slip condition would initiate when the resultant force is larger than zero. For a system under base excitation vibration, the force exerted on the vibrating mass is equal to the base input force. Hence, the stick condition of a base-excited vibrating system with a dynamic friction surface is

$$|F| = k_pY \mp F_R < 0 \tag{13}$$

where $|F|$ is the resultant force between the force exerted on the base and the friction force. Notice that Eq. (13) corresponds to the right hand side of Eqs. (1) and (2) under steady-state condition. The slip condition would then be

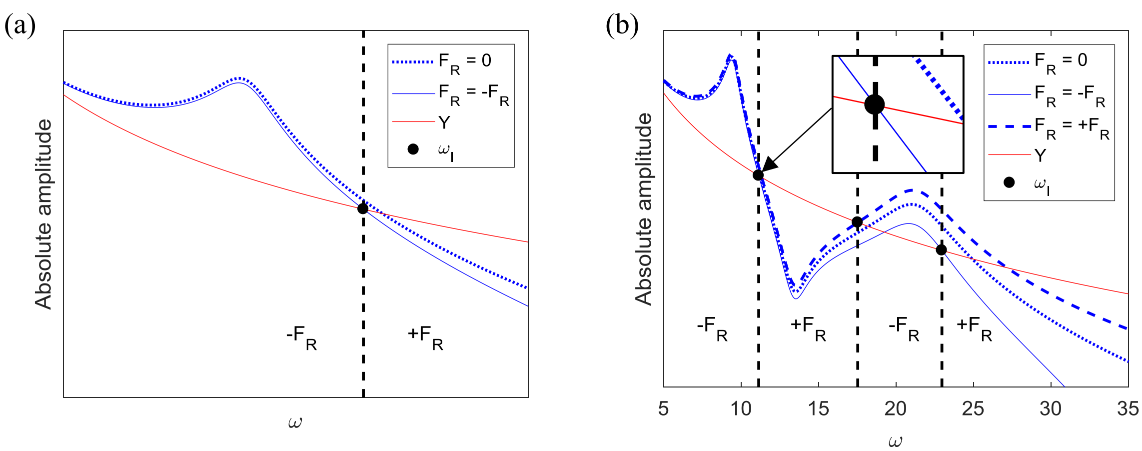

Fig. 4. Correct method in evaluating the isolations freqeuncies of a (a) SDOF and (b) 2DOF system.

$$|F| = k_pY \mp F_R > 0 \tag{14}$$

Base on Eqs. (13) and (14), it can be deduced that the stick condition would only occur when F_R is negative. This means that for the case of a SDOF system under base excitation vibration with a dynamic friction surface, the sticking condition would not occur provided that the magnitude of k_pY is larger than F_R at frequencies lower or equal to ω_I, since a SDOF system only has a single isolation frequency and after ω_I, F_R is always positive. In the case of a static friction surface, the sign for F_R would always be negative, indicating that it always oppose the exerted force. Fig. 5 shows the slip-stick region of the 2DOF system illustrated in Fig. 1 for the case of a dynamic and static friction surface.

It can be seen that the static friction surface case is more prone to sticking as compared to the dynamic case. Theories 1 and 2 predicts different frequencies at where sticking begins due to the difference in their assumptions. One of main difference between the stick condition for a dynamic friction surface and a static friction surface is that the mass in contact would theoretically remain stationary if it sticks to a static friction surface. However, since the dynamic friction surface vibrates together with the vibrating base, this would cause the mass in contact to remain vibrating under the stick condition. Depending on application, this condition may or may not be desirable.

2.3. Mathematical model of cantilever beam with lumped mass under harmonic base excitation

Consider the case of a clamp-free cantilever beam with a lumped mass attached on its free-end, subjected to a base excitation motion as illustrated in Fig. 6.

Here, E, I, ρ, m and L represents the Young's modulus, second moment of area, density, mass and length of the cantilever beam whereas m_t, i_t and s_t are the mass moment of inertia and static moment of the lumped mass at position $u = L$. The transverse motion of the beam at position x and time t can be described by the following equation.

$$v_{abs}(u,t) = v_{rel}(u,t) + v_0 e^{i\omega t} \tag{15}$$

where $v_{abs}(u,t)$ is the absolute vertical displacement of the beam, $v_{rel}(u,t)$ is the vertical displacement beam relative to its vibrating base and v_0 and ω are the vertical amplitude and vibrating frequency of the harmonic base excitation. In most vibration energy harvesting applications, the geometry of the beams used allows it to be modelled from the Euler-Bernoulli theory. Using the method of separation of variables, the term $v_{rel}(u,t)$ can be separated into its spatial and temporal components [26].

$$v_{rel}(u,t) = \sum_{n=1}^{\infty} \varphi_n(u)\eta_n(t) \tag{16}$$

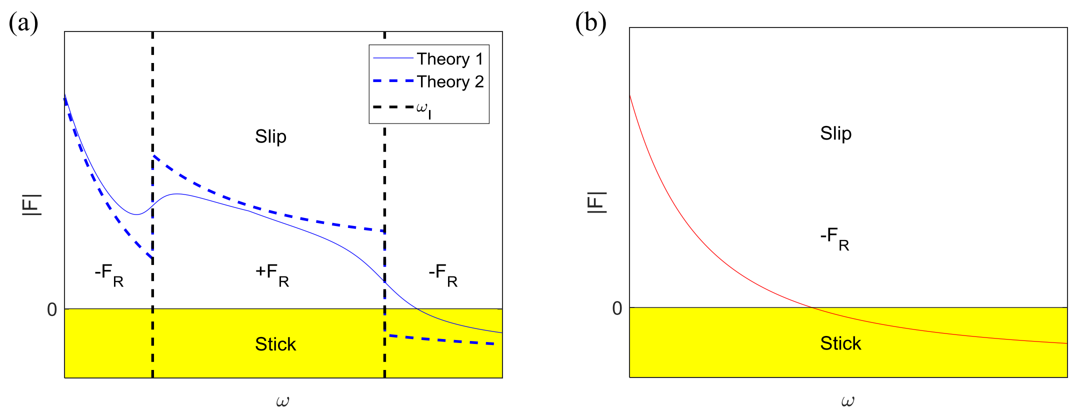

Fig. 5. Slip-stick condition for a 2DOF system subjected to a (a) dynamic friction surface and (b) static friction surface.

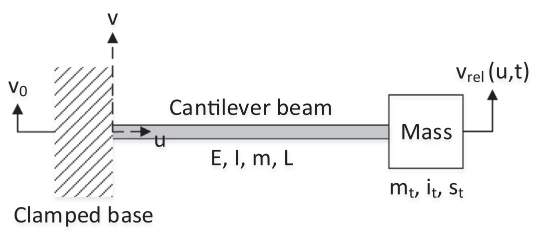

Fig. 6. Cantilever beam with a lumped mass placed on the free-end of the beam.

where $\varphi_n(x)$ is the modal shape function of the beam and $\eta_n(t)$ is the regular-response function. These terms can be described as the following equations

$$\varphi_n(u) = K_n\left[\cosh\frac{\lambda_n}{L}u - \cos\frac{\lambda_n}{L}u - \frac{J_1}{J_2}\left(\sinh\frac{\lambda_n}{L}u - \sin\frac{\lambda_n}{L}x\right)\right] \tag{17}$$

$$\eta_n(t) = \frac{\omega^2 v_0 e^{i\omega t}F_n}{\omega_n{}^2 - \omega^2 + i2\zeta_n\omega_n\omega} \tag{18}$$

$$F_n = \frac{m}{L}\int_0^L \varphi_n(u)du + m_t\varphi_n(L) + s_t\frac{d\varphi_n}{du}(L) \tag{19}$$

$$\frac{1}{K_n{}^2} = \frac{m}{L}\int_0^L [\tau_n(u)]^2 dx + \tau_n(L)\left[m_t\tau_n(L) + s_t\frac{d\tau_n}{dx}(L)\right] + \frac{d\tau_n}{dx}(L)\left[i_t\frac{d\tau_n}{dx}(L) + s_t\tau_n(L)\right] \tag{20}$$

$$\tau_n(u) = \frac{\varphi_n(u)}{C_n} \tag{21}$$

where ζ_n corresponds to the modal damping ratio of the beam and λ_n and $\frac{J_1}{J_2}$ are constants that can be determined from the boundary conditions of the beam-mass system [27]. Substituting Eqs. (17) and (18) into Eq. (16) and considering only the first mode parameters at resonance ($\omega = \omega_1$) results in

$$v_{rel}(u,t) = \frac{v_0 e^{i\omega_1 t}\varphi_1(u)}{2\zeta_1}F_1 \tag{22}$$

To evaluate the vertical displacement of the beam after $u = L$, the following extrapolation can be applied

$$v_{rel}(u > L, t) = \frac{v_0 e^{i\omega_1 t}\varphi_1(L)}{2\zeta_1}F_1 + (u - L)\frac{\partial\varphi_1(u)}{\partial u}\bigg|_{u=L} \tag{23}$$

Subsequently, the phase angle of a vibrating beam, θ_b, can be determined from the denominator of Eq. (18), resulting in the similar form to Eq. (12).

$$\theta_b = \tan^{-1}\left(\frac{2\omega\omega_n\zeta_n}{\omega_n{}^2 - \omega^2}\right) \tag{24}$$

2.4. Voltage output and damping evaluation methods

Based on Faraday's law of electromagnetic induction and Kirchhoff's voltage law, the root-mean-square (RMS) peak voltage produced at the load resistor when the vibrating coil cuts through a magnetic field is described by Eq. (25).

$$V_L = \frac{1}{\sqrt{2}}N_c B l_c A_{rel}\omega f\frac{R_L}{R_L + R_c} \tag{25}$$

where V_L is the induced RMS peak voltage across the load resistance R_L, N_c is the number of turns of coil, B is the average magnetic flux, l_c is the effective length of the coil, A_{rel} is the amplitude (peak displacement) of the vibrating coil relative to the magnets, f is the coil fill factor [28] and R_c is the coil resistance. Under the same base excitation motion, A_{rel} can from the following equation

$$A_{rel} = \sqrt{A_c{}^2 + A_m{}^2 - 2A_cA_m\cos(\theta_c - \theta_m)} \tag{26}$$

where A_c and A_m are the absolute amplitudes of the vibrating coil and magnets and θ_c and θ_m are their respective phase angles. Applying ohm's law, the peak power output at the load resistance can then be calculated by

$$P_L = \frac{V_L{}^2}{R_L} \tag{27}$$

One of the main issue in vibrations is on the damping evaluation of the vibrating system. Normally for an electromagnetic vibration energy harvester, there are two dominant sources of damping which are the mechanical damping and the electromagnetic damping [29]. In this study, the mechanical damping ratio for the spring-mass system was determined from experiment. However, the mechanical damping ratio for the cantilever beam was obtained using the critically damped stress method proposed by Foong et al. [30,31], with the following damping stress equation for first mode vibrations of stainless steel beams

$$\zeta_m = 2.109 \times 10^{-8}\sigma_{cr}{}^{0.8447} + 0.001662 \tag{28}$$

where σ_{cr} is described as twice the stress at the clamped end of the beam under resonance and critically damped condition ($\zeta_1 = 1$). For first mode vibrations, this value can be approximated by

$$\sigma_{cr} = Ehu_0\left(\frac{\beta_1}{L}\right)^2 K_1 F_1 \tag{29}$$

where h is the thickness of the beam. Note that for macro sized structures, the air damping and thermo-elastic loss of stainless steel can be considered negligible [30]. The electromagnetic damping for both the spring-mass system and the cantilever beam can be estimated from Eq. (30) [32].

$$\zeta_e = \frac{(NBlf)^2}{2m_{eq}\omega_n(R_c + R_L)} \tag{30}$$

where ζ_e is the electromagnetic damping and m_{eq} is the equivalent mass of the structure. Therefore, the total damping of an electromagnetic harvester is equal to the sum of Eqs. (28) and (30) [1,33,34].

$$\zeta_1 = \zeta_m + \zeta_e \tag{31}$$

3. SDOF cantilever beam-based electromagnetic vibration energy harvester

In this section, the voltage output of a conventional cantilever beam-based vibration energy harvester shown in Fig. 7 was simulated and experimentally recorded. The results in this section would be used to verify the analytical equations and compared to the 2DOF and 2SDOF design. The 2DOF and 2SDOF designs are simply the modified version of Fig. 7 through the addition of a spring component, while maintaining the same overall volume.

The design in Fig. 8 consist of a stainless steel cantilever beam with a coil attached on one end and clamped to the base on the other end. Two pairs of magnets were fixed onto the magnet holder and clamped onto the base. A steel plate was also placed behind the magnets to concentrate the magnetic field in the air gap between them [8]. Voltage is generated when the

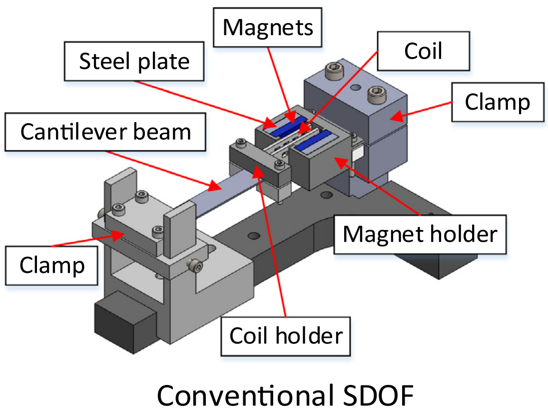

Fig. 7. Conventional cantilever beam-based electromagnetic vibration energy harvester.

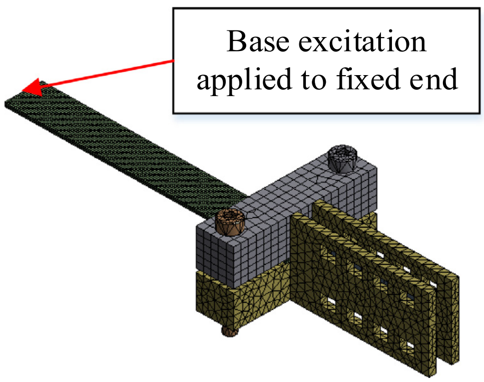

Fig. 8. Finite element model mesh and boundary conditions of a conventional SDOF harvester.

beam vibrates causing a change in magnetic flux as the coil to cuts through the magnetic field of the magnets. Since there are no relevant surface contacts, frictional interactions are not required to be modelled.

3.1. FE modelling of SDOF cantilever beam-based electromagnetic vibration energy harvester

The cantilever beam and coil was modelled and simulated in ANSYS Workbench 17.2 as a clamp free cantilever beam using a 20-node SOLID186 quadratic elements with a 0.50 mm element size for the beam and a 2 mm element size for other components. A fixed boundary condition was applied to the clamped end of the beam. The mechanical damping ratio of the beam was evaluated by performing a harmonic analysis on the FE model using a damping ratio input of $\zeta_m = 1$ and a base acceleration input of $G = 0.30\,g$ ($1\,g = 9.81\ \mathrm{ms}^{-2}$). The value of σ_{cr} was then determined from the first mode resonance of the simulated results and substituted into Eq. (28) to obtain the actual value of ζ_m. The electromagnetic damping, ζ_e, was simply calculated from Eq. (30), in where the equivalent mass of the structure, m_{eq}, was obtained from the FE model. The harmonic analysis was then repeated using the same base acceleration input and a damping ratio value equal to the sum of ζ_m and ζ_e. The simulation was then repeated for a base acceleration input of 0.35 g, 0.40 g, 0.45 g and 0.50 g. The properties of the coil and the beam for each different base acceleration magnitude is listed in Table 1.

Since the magnets are directly clamped to the base, their vibrating amplitude and phase is assumed equal to the vibrating base. Hence, the magnet vibrations were not simulated. The mesh and boundary conditions of the cantilever beam FE model is illustrated in Fig. 8.

Technically, the amplitude of a vibrating beam would vary with position u. In this study, the average amplitude of the entire coil is assumed to be equal to the amplitude at the centre of the coil. This position was measured to be at $u = L+$ 32.05 mm. As the magnets are fixed to the vibrating base, the absolute amplitude of the magnets, A_m, is equal to the amplitude of the vibrating base. Therefore, the amplitude of the coil relative to the magnets, A_{rel}, would correspond to the amplitude of the coil relative to the vibrating base. In the FEA simulation, ANSYS Workbench outputs the base relative amplitude of a vibrating object at any desired position on the FE model for a set frequency range when using the harmonic analysis step. This means that the peak voltage output can be directly determined by substituting the simulation results into Eq. (25).

3.2. Experimental verification and discussion of SDOF cantilever beam-based electromagnetic vibration energy harvester

An experiment was performed to validate the FE model and the theoretical equations. The design in Fig. 7 was fabricated and fixed onto an LDS V406 electromagnetic shaker as shown in Fig. 9.

The shaker was controlled using an analogue output NI-USB 6341 function generator and a closed loop feedback system was created using an accelerometer (500 mV/g). The feedback accelerometer was connected to an analogue input NI 9229 data acquisition card (DAQ), which is connected to the computer and controlled through LabVIEW. The induced voltage generated is also connected to the same DAQ. The displacement of the vibrating coil was captured using a separate system consisting of a Fiber optic MTI 2100 fotonic sensor. The experiment was conducted for the same five base acceleration magnitude as the FEA simulation. The amplitude of the coil at $u = L+$ 32.05 mm and the peak to peak load voltage was recorded for each experiment. The amplitude values recorded from experiment relates to the absolute amplitude. Fig. 10 shows the results of the coil's absolute amplitude, A_c, and the RMS peak voltage at the load resistor, V_L for theory, FEA simulation and experiment.

Eq. (26) was applied to determine the absolute amplitude of the coil for the theoretical and simulation results. The experiment results recorded a natural freqeuncy of 29.2 Hz whereas the theoretical and simulation results recorded a natural freqeuncy of 29.1 Hz and 29.2 Hz respectively. This result in an error of less than 1.0%. In terms of the base relative amplitude and load voltage, the theoretical results displayed a maximum error of 16.0% with respect to the experimental results for an acceleration level of 0.3 g. It can be concluded that a good agreement can be observed for all plotted results in Fig. 10 in terms of trend and values. This hence verfies the FE model and the theoretical equations applied in this study. Additionally, the results also validates the mechanical damping evaluation method for cantilever beams applied here.

Table 1
Properties of cantilever beam for the FE model.

Coil		Cantilever beam					
N_c	250	G (g)	0.30	0.35	0.4	0.45	0.50
B (T)	0.26	E (GPa)	180	180	180	180	180
l_c (mm)	44	I (mm^4)	0.833	0.833	0.833	0.833	0.833
R_c (Ω)	6.5	h (mm)	1.0	1.0	1.0	1.0	1.0
R_L (Ω)	22.0	L (mm)	65.0	65.0	65.0	65.0	65.0
f	0.65	ρ (kgm^{-3})	7788.5	7788.5	7788.5	7788.5	7788.5
		m_{eq} (g)	22.98	22.98	22.98	22.98	22.98
		σ_{cr} (MPa)	3.730	4.352	4.974	5.595	6.217
		ζ_m	0.0092	0.0102	0.0112	0.0122	0.0132
		ζ_e	0.0146	0.0146	0.0146	0.0146	0.0146

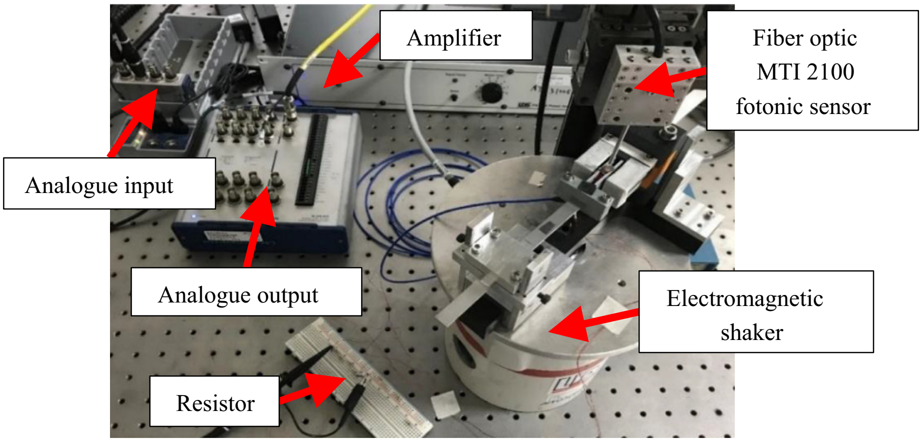

Fig. 9. Experiment setup to determine the voltage output of a conventional electromagnetic harvester.

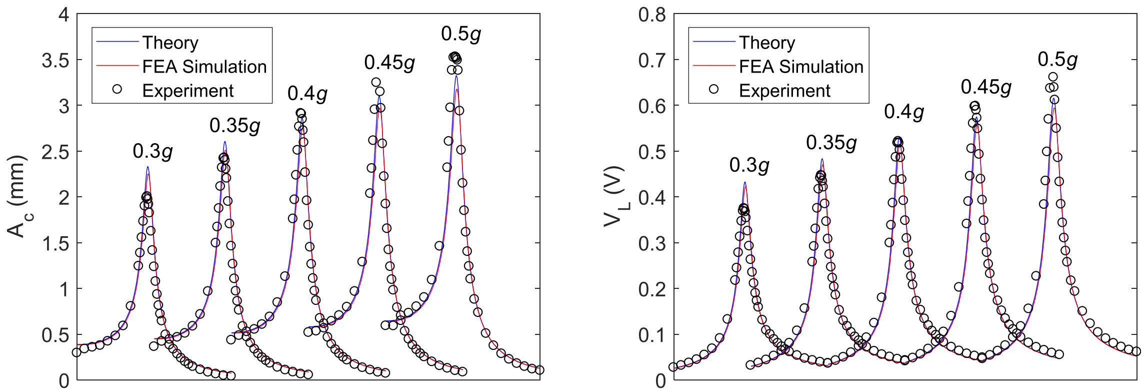

Fig. 10. Absolute coil amplitude and peak voltage comparison between theory, FEA simulation and experiment.

4. Modification to 2SDOF system through spring addition

One of the main disadvantages of the conventional SDOF cantilever beam harvester is its limited operational frequency range. Generally, useful power is only generated when the system vibrates at or very close to its resonant frequency. To overcome this drawback, a spring was introduced into the conventional SDOF design, replacing the clamp used to clamp the magnets as seen in Fig. 11. This will cause both the coil and the magnet to vibrate when the base vibrates. Note that the overall volume of the conventional SDOF design is maintained.

The modified design is basically a 2DOF system consisting of two SDOF structures. Since the vibration of the coil and the magnets are independent to each other, this design will be referred to as a 2SDOF design. A mechanical slider (HIWIN MGW9C

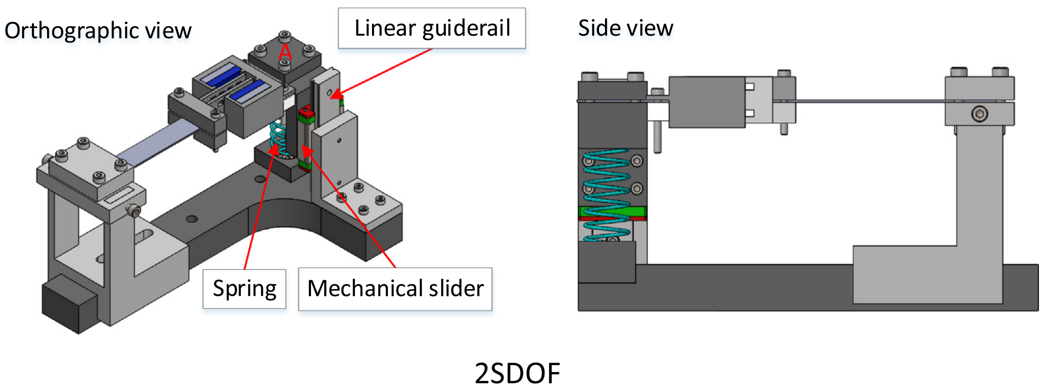

Fig. 11. Design of a 2SDOF electromagnetic vibration energy harvester.

model) and a linear guiderail was used to ensure that the magnet and spring only vibrates in the vertical direction. This unavoidably introduced a small friction into the system. The preload between the mechanical slider and the linear guiderail was given as 55 N [35] and the friction coefficient between these two components was determined to be $\mu = 9.8 \times 10^{-4}$. This friction coefficient correlates to the kinetic friction coefficient. The static friction coefficient was not considered as the static friction would have converted to kinetic friction when steady-state vibration is achieved. Since the mechanical slider is positioned vertically, it is acceptable to assume that the preload and the friction coefficient between the slider and the guiderail is independent of the mass attached to the slider, ensuing a constant frictional force magnitude of $F_R = 0.054$ N.

The stiffness of the added spring was determined using Eq. (32) based on the properties of a fabricated spring.

$$k = \frac{d_i^4 E_s}{8 d_o^3 N_s} \tag{32}$$

where d_i is the diameter of the spring wire, E_s is the shear modulus of the spring material, d_o is the outside diameter of the turn and N_s is the number of active turns of the spring. These values are tabulated in Table 2, resulting in a spring stiffness of 1017.8 Nm^{-1}. The mechanical damping ratio of the spring (without friction) was obtained from experiment using the logarithmic decrement method based on the voltage reading as shown in Fig. 12 [36], resulting in a damping ratio of 0.0454. The electromagnetic damping of the design was determined from Eq. (30) and its respective damping constant was then obtained using Eqs. (6) and (31). It is worth to mention that the initial constant voltage value in Fig. 12 was due to a large initial displacement that exceeded the limitations of the fiber optic sensor, which have a maximum working range of approximately ± 4.0 mm.

4.1. FE modelling of 2SDOF design

Since the coil and magnets in the 2SDOF design can act as two individual systems, they can be simulated separately, provided that both the mechanical and electromagnetic damping are considered in the separate simulations. In addition, the voltage output of the 2SDOF system must be determined based on the relative amplitude between the coil and the magnets. Similar to before, the vibration of the cantilever beam with coil was simulated in ANSYS Workbench 17.2 under a constant base excitation acceleration of 0.3 *g* using the same cantilever beam properties and dimensions as in Table 1. The simulation of the beam was conducted for a total of three cases to observe the effect of natural frequency reduction on the behaviour of the design. Here, Case 3 corresponds to the configuration illustrated in Fig. 7 and Case 2 and Case 1 correspond to the configurations where additional masses, m_a, weighing 36.80 g and 87.55 g were added onto the coil holder to reduce the natural frequency of the beam. The base excitation acceleration was kept at 0.3 *g* for all three cases. It is easy to notice that the vibrating coil simulation for Case 1 has actually been conducted in the previous section. For Cases 2 and 3, the additional masses were modelled added as block masses to replicate available materials.

The vibration of the magnet component was modelled in ABAQUS 2018 due to the reason that convergence issue for nonlinear contact problems are more resolved in the latest version of ABAQUS [37], resulting in a significantly shorter simulation time. These components were modelled as a simplified two dimensional SDOF spring mass system using CPS4R (a 4-node bilinear plane stress quadrilateral, reduced integration, hourglass control) elements with a mesh size of 0.25 mm for the mass and 0.50 mm for the base. The simplification was made to reduce computational time. The masses of the magnets, magnet holder, clamp and mechanical slider were represented by Mass 0 in Fig. 14, in which Mass 0 is a square geometry measuring 10×10 mm with a density value that reflects the equivalent summed mass of all the said components. An L-shaped geometry was modelled for the base, ensuring that the tall side of the base makes contact with the Mass 0. A spring and dashpot element was added to connect Mass 0 to the base. A boundary condition was applied to the base to constrain it in the horizontal direction. The friction between the mechanical slider and the linear guiderail was defined in the form of a surface friction between Mass 0 and the tall side of the base in the FE model. A general frictional interaction with a defined friction coefficient of 9.8×10^{-4} was assigned to the FE model. A pressure load was applied to the mass to generate a normal force that is equal to the 55 N preload [35].

Table 2
Properties of the magnet-spring and cantilever beam component for the 2SDOF FE model.

Magnets and Spring		Cantilever beam			
			Case 1	Case 2	Case 3
d_i (mm)	1.5	m_a (g)	87.55	36.80	0.00
E_s (GPa)	69	m_{eq} (g)	87.73	54.67	22.98
d_o (mm)	18.3	σ_{cr} (MPa)	14.772	8.597	3.730
N_s	7	ζ_m	0.0257	0.0169	0.0092
k (Nm^{-1})	1017.8	ζ_e	0.0082	0.0093	0.0140
m_{eq} (g)	217.56	ω_n (Hz)	13.4	18.9	29.2
ζ_m	0.0454				
ζ_e	0.0041				
c (Ns m^{-1})	1.48				

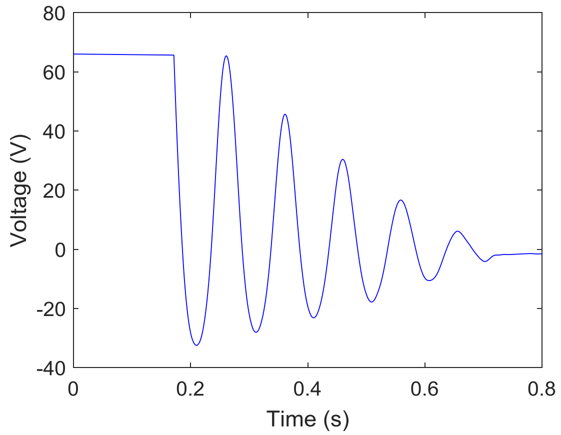

Fig. 12. Logarithmic decrement plot of spring mechanical damping ratio.

A transient analysis was performed in ABAQUS using the dynamic implicit analysis step by defining a sinusoidal base excitation input corresponding to an acceleration of 0.3 g at the bottom of the base. The amplitude of the sinusoidal base input was determined from Eq. (4). Fig. 13 describes the mesh and boundary conditions of the FE model for the magnet component in the 2SDOF design.

The simulation of the magnets and spring component was only conducted once due to the fact that the configuration remained the same in all three cases. Table 2 tabulates the specifications of the 2SDOF design for Cases 1, 2 and 3.

Since a transient analysis was performed using a dynamic implicit step in ABAQUS, the output amplitude of the vibrating mass obtained from the simulation would relate to the absolute amplitude of the FE model. The voltage output of the simulation was then calculated using Eqs. (25) and (26).

4.2. Experimental verification and discussion of 2SDOF design

An experiment was carried out using the same apparatus as in Fig. 5 for Cases 1, 2 and 3 to validate the FEA simulation results and the analytical equations in Section 2. In the experiment, the peak to peak voltage generated by the design and the absolute amplitude at position **A** in Fig. 11 were recorded. For this design, the recorded absolute amplitude correspond to the absolute amplitude of the vibrating magnets. Fig. 14 displays the comparison between experiment, FEA simulation and theory for the absolute amplitude of at position **A**, A_A, and also the peak RMS load voltage, V_L, for all three cases. Under the given input base acceleration, the magnitude of the input force, k_pY, was determined to be larger than the friction force, F_R, at frequencies below ω_I. Hence, the stick condition would not be predicted by the theoretical equations. The difference due to the assumptions made in Theory 1 and Theory 2 are highlighted in the zoomed in section for each plot. The first peak in the load voltage plots for all three cases corresponded to the first mode resonance of the magnets whereas the second peak corresponded to the fundamental resonance of the coil.

Results in Fig. 14 shows a strong agreement between the theoretical calculations and FEA simulation. The isolation freqeuncies, ω_I were determined to be at 14.7 Hz for all three cases, hence signifying a sudden increase or decrease in voltage at these regions for when Theory 2 was applied. However, it is observed that the simulation results agree more with Theory 1,

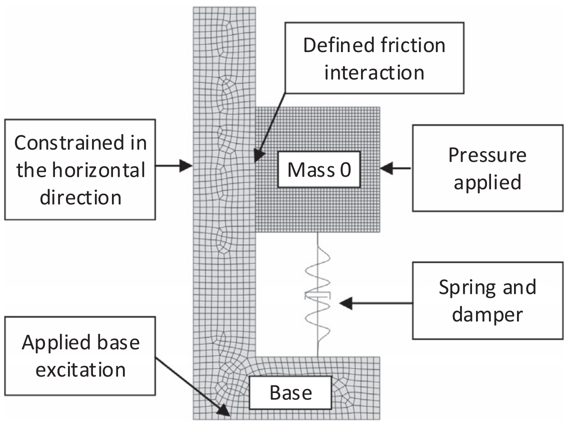

Fig. 13. FE model mesh and boundary conditions of the magnet component in 2SDOF design.

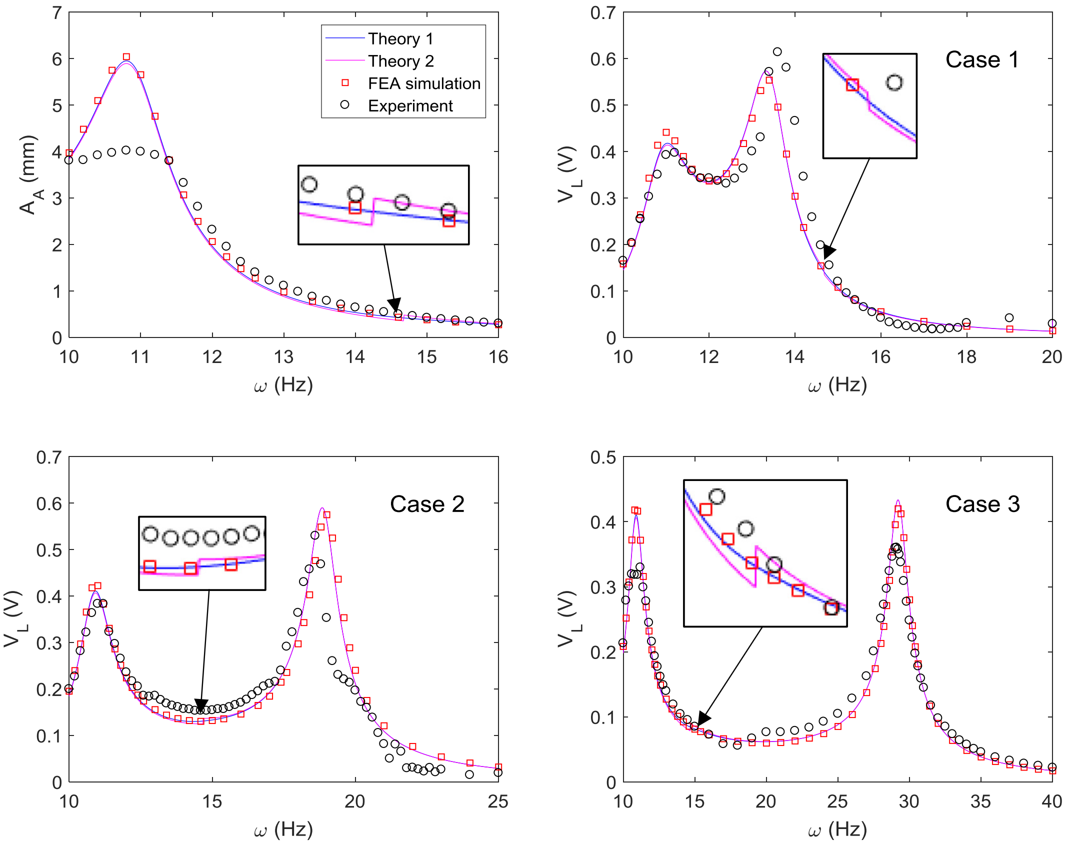

Fig. 14. Absolute amplitude of a point A and RMS peak voltage output for Cases 1, 2 and 3 of 2SDOF design.

as there are no sudden changes in amplitude or voltage from the simulation results. The reason for this is due to the FEA program itself. Discontinuities are observed in Theory 2 as the change in friction direction was assumed to be instantaneous, making it impossible to solve analytically. Hence, the FEA software modifies the Coulomb friction model so that the change in friction direction is more delayed, instead of instantaneous. At this point, it is unclear as to which theory assumption agrees more with the experimental results, as the differences between Theory 1 and Theory 2 are very small and may not be reflected properly in the experiment. It can be seen that the experimental results for the absolute amplitude of the magnets is significantly lower than the theoretical and FEA results at its peak value. This is due to the limitation of the fibre optic sensors used in the experiment as mentioned earlier. Hence, any amplitude higher than this range will not be captured properly by the sensors. Nevertheless, a good agreement can be seen between the experimental results and both analytical results in terms of voltage output for all three cases, suggesting that the FEA simulation and the theoretical equations are correct.

One of the main advantage of the 2SDOF design as compared with the conventional SDOF design is the presence of two operational resonant freqeuncy. This means that useful power can be generated under two different freqeuncy ranges. The addition of the spring in the conventional SDOF design causes both the coil and the magnets to vibrate, resulting in two distinct voltage peaks corresponding to the first mode resonance freqeuncy of the magnets and the coil. In addition, the voltage between the these two peaks was also improved due to the anti-phase motion between the coil and the magnets within this region, resulting in a greater relative amplitude. This improvement is more obvious when the two resonant freqeuncies are closer to each other as seen in Case 1, resulting in an increase in the operational freqeuncy bandwidth. In terms of voltage output, Case 1 recorded the highest power output at the second peak, which is mostly due to the decrease in the resonance freqeuncy of the coil from the additional mass. Nevertheless, if Case 3 was to be compared with the conventional SDOF design for the same base input of 0.3 g, the maximum peak voltage for both designs are very similar. Hence it can be concluded that while the 2SDOF design can enhance the bandwidth of an electromagnetic harvesters, it produces the same maximum peak voltage as that of a conventional SDOF design.

5. Modification to 2DOF system through spring addition

Similar to the 2SDOF design, a spring was introduced into the conventional SDOF design to overcome its limitations while maintaining the same volume. This time, the spring was fixed to the base of the cantilever beam whereas the magnets were clamped onto the vibrating base as seen in Fig. 15.

This new design is similar to the 2SDOF design in terms that both designs represent a 2DOF system. However, the vibration of the coil and the spring in this design are not independent to each other, in where the vibration of the spring in greatly influenced by the stiffness and the damping of the cantilever beam. Therefore, this design will be referred to as a 2DOF design. The same frictional force of F_R = 0.054 N was also assumed for this design. Since the same spring was used, the stiffness of the spring remains the same. However, the mechanical damping ratio of the spring was experimentally re-determined to be equal to 0.080.

5.1. FE modelling of 2DOF design

The 2DOF design in Fig. 15 was simplified into an equivalent 2DOF spring mass system as seen in Fig. 1 and modelled in ABAQUS. The FE model of the 2DOF design is similar to Fig. 13, except that a second mass was added on top of the Mass 1 and connected to Mass 1 with a spring and dashpot element as seen in Fig. 16. The geometry of Mass 2 was modelled smaller than Mass 1 to avoid any contact with the tall side of the L-shaped base. Mass 2 represents the equivalent mass of the cantilever beam, coil holder and coil whereas Mass 1 represents the equivalent mass of the clamp and mechanical slider. Their respective spring and dashpot elements corresponds to the stiffness of the components. The same element type, friction def-

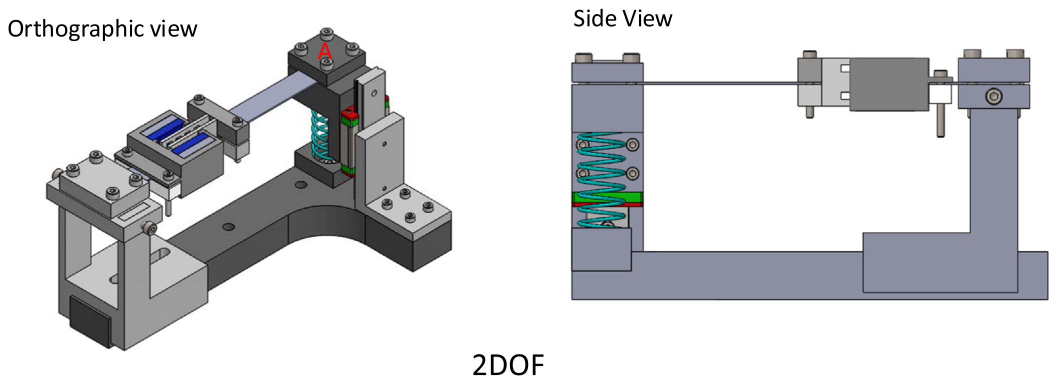

Fig. 15. Design of a 2DOF electromagnetic vibration energy harvester.

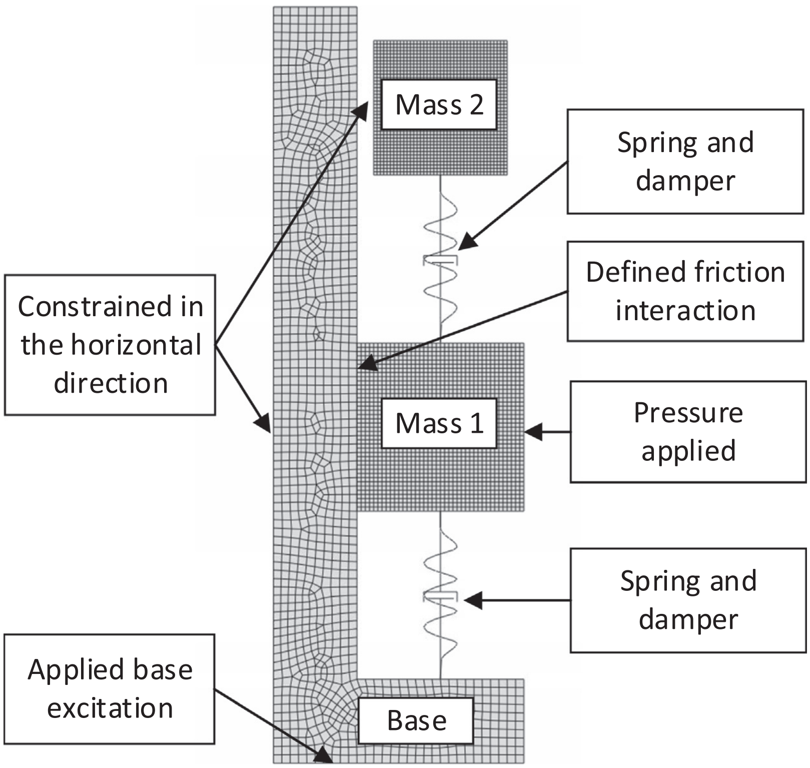

Fig. 16. FE model mesh and boundary conditions of the 2SDOF design.

inition, mesh sizes and boundary conditions as the 2SDOF model were applied here, with an additional constraint applied on Mass 2 to restrain its motion in the horizontal direction. In addition, the same three cases as the 2SDOF design was also analysed for this design.

Table 3 describes the stiffness, damping and equivalent masses applied to Mass 1 and Mass 2 in the 2DOF FE model. The mechanical damping ratio of the cantilever beams for all three cases were assumed to be equal to that of the 2SDOF design. However, the electromagnetic damping ratios will differ according to the natural frequency of the design. The mechanical damping ratio of the spring was assumed constant for all three cases.

A transient analysis was performed on the FE model using the dynamic implicit step and the absolute amplitude of Mass 2 was recorded at different frequency intervals. The voltage was then calculated based of the relative amplitude of Mass 2 with respect to the vibrating base.

5.2. Experimental verification and discussion of 2DOF design

The previous experiment was repeated for the 2DOF design by exchanging the position of the magnets and the cantilever beam. The peak to peak voltage of the design and the absolute amplitude of point A was recorded for different frequency intervals. Fig. 17 shows the comparison between experiment, theory and FEA simulation results. In the analytical results, the sticking effect was not predicted in all three cases for the given frequency range. The differences between Theory 1 and Theory 2 are highlighted in the zoomed in section for all plots. A good agreement can be seen between the theoretical, FEA simulation and experimental results for all cases.

Case 3 recorded a single isolation frequency whereas Case 1 and Case 2 recorded three and two isolation frequencies respectively. Due to the limitations of the fibre optic sensor stated earlier, the experimental absolute amplitude for Case 1 could not be recorded properly. In addition, it is observed that the experiment results may have experienced a certain degree of the stick-slip phenomena which may suggest that the friction force fluctuates in the experiment. Similar to before, the FEA simulation results agree strongly with Theory 1. It is seen that increasing the mass on the beam reduces both the first and second mode frequencies of the 2DOF system, resulting in the highest maximum voltage output for Case 1. Another observation made here is the presence of other observable peaks after the first resonance peak in the experimental voltage output, which is more clearly observed in Case 2 and 3. In addition, this peak was also observed in the experimental absolute amplitude at point A for Case 3. These peaks were not predicted by the FEA simulation. The peaks do not correspond to any resonant frequency, but occurs around the isolation frequencies. This suggest that the change in friction force direction in the experiment was more sudden, hence agreeing more with Theory 2 although the change in the experiment was not as abrupt as the assumption made in Theory 2. This shows that in practical, friction changes can be more abrupt due to the fact that while the magnitude of the friction force may fluctuate in the experiment, it is relatively independent to the motion of the mass in contact and cannot reach zero. Therefore, it is impossible for experimental friction to experience a delayed transition in friction force as assumed in Theory 1. The voltage value predicted by the theoretical equations and FEA simulation are observed to be somewhat lower than the experimental results, especially after the first mode resonance. This is due to the simplification made in converting the coil and cantilever beam into a spring and mass system representation. The amplitude output of a spring mass system corresponds to the amplitude of the cantilever beam at $u = L$, whereas the voltage output was determined to agree with the amplitude at the centre of the coil at $u = L+$ 32.05 mm. The amplitude at $u = L+$ 32.05 mm is highly dependent on the free end deflection gradient of the vibrating beam. Therefore, at lower freqeuncies, the theoretical and simulation results agrees more with the experimental results as the beam does not deflect significantly. However, as the beam approaches the second mode, it deflects more resulting in a larger difference between the amplitudes at $u = L$ and $u = L+$ 32.05 mm. In addition, the electromagnetic damping at this region would also be lower due to the increase in modal frequency.

Due to the change in the direction of the friction force at the isolation frequencies for a dynamic friction surface, it may be possible to tune the behaviour of the harvester's voltage output by adjusting the friction force. Fig. 18 describes the effect of a dynamic and static friction surface on the absolute amplitude (at position **A)** and the voltage output for Case 3 under three different friction force. Here, Theory 2 was applied. An assumption was made in that under the stick condition, the mass in contact would vibrate with the friction surface for the dynamic friction surface and remains stationary for the static friction surface. Therefore, Mass 2 would vibrate as a SDOF system under base excitation at the stick region for the dynamic friction surface case. The dynamic friction surface predicted the stick condition only when F_R = 0.150 N whereas the static friction surface predicted sticking when F_R = 0.054 N and F_R = 0.150 N. The number of isolation frequency increased to two when a friction force of F_R = 0.150 N was applied to the dynamic friction surface case.

It can be seen that as the friction force increases in the dynamic friction case, the voltage output before the first isolation frequency decreases whereas the voltage output after this frequency increases. At the isolation frequency itself, the voltage output increased considerably, resulting in three significant voltage peaks when F_R = 0.150 N. This trend was not observed in the static friction surface case. For this case, the voltage at both resonance peaks would decrease with increasing friction. In addition, the frequency at where sticking begins also decreased with increasing friction force, hence decreasing the range of frequencies where voltage can be generated. The results suggest that the 2DOF design can achieve more significant voltage peaks by tuning the friction force of the dynamic friction surface. If Case 3 was compared to the conventional SDOF design, the 2DOF design would actually result in a lower maximum peak voltage at its first resonance peak, despite having a lower natural frequency value even for the case of no friction. However, this is mainly due to the increase in the overall damping.

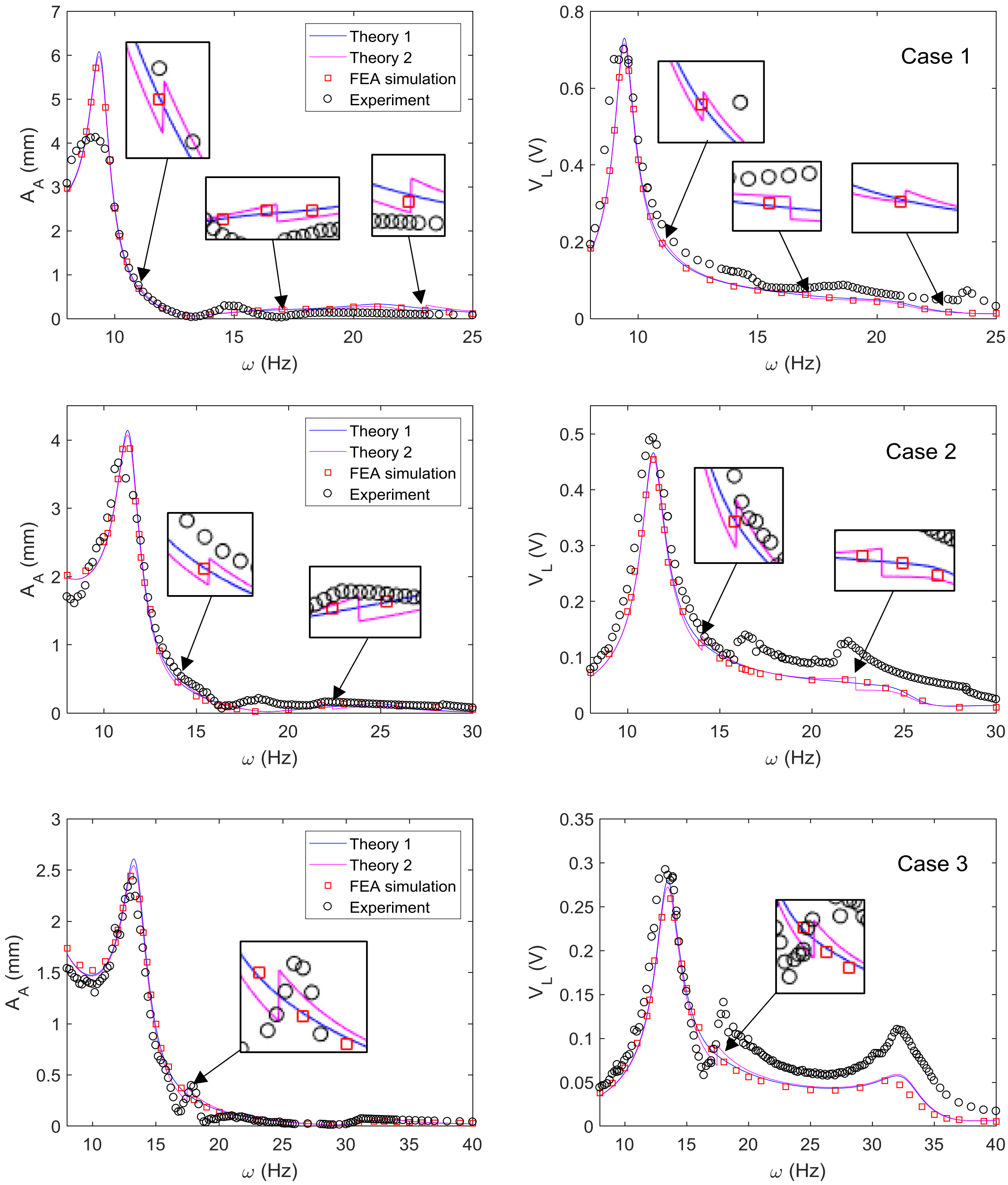

Fig. 17. Absolute amplitude of a point A and RMS peak voltage output for Cases 1, 2 and 3 of 2DOF design.

Table 3
Properties of Mass 1 and Mass 2 for the FE 2DOF model.

	Mass 1	Mass 2		
		Case 1	Case 2	Case 3
k (Nm^{-1})	1017.8	621.87	770.96	774.66
c (Ns^{-1})	1.72	0.57	0.42	0.34
m_{eq} (g)	113.12	87.73	54.67	22.98

6. Power output and power density comparison between SDOF, 2SDOF and 2DOF.

In this section, the theoretical peak power output at the load resistance and power density between the conventional SDOF cantilever beam design and the 2SDOF and 2DOF design will be compared for all three cases under a base acceleration

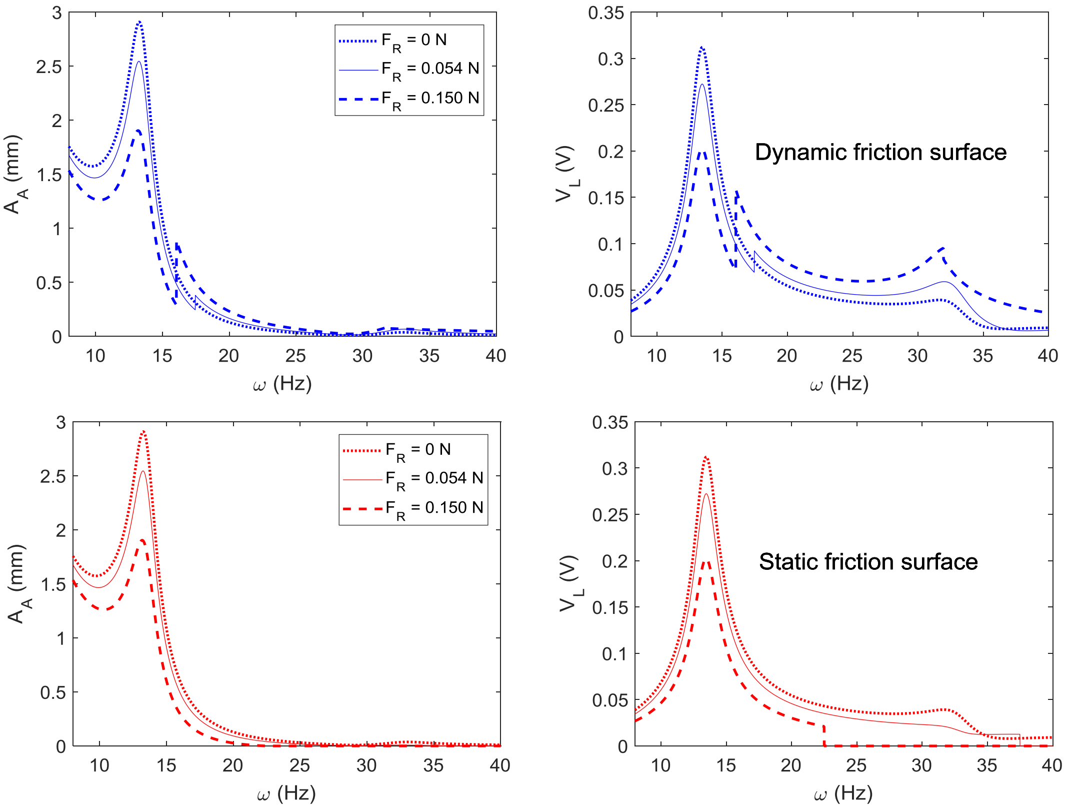

Fig. 18. Comparison between a dynamic friction surface (blue) and a static friction surface (red) for Case 3.

input of 0.3 g. Generally, different harvester designs would have a different optimum load resistance value (R_L^{opt}) that correspond to its maximum power output [38–40]. Previously, the experiment was conducted using an arbitrary load resistance value of 22.0 Ω. However, the analysis conducted here considered the condition of optimum load resistance, which was determined by plotting the maximum peak power output against R_L.

Usually, the power density of a harvester is defined as the ratio of its maximum power output to its volume and base acceleration input [41]. By default, all three designs would have approximately the same overall volume since the same setup was used. However, it is more appropriate to consider the practical volume of the harvester. This volume includes the space occupied by the harvester during its peak vibration. The solid blue outline in Fig. 19 indicates the actual volume of the harvester and the dashed outline is the additional volume that must be considered for the design's practical volume.

Based on Fig. 19, the practical volume of the harvester, V_p, for each design can be defined as

$$V_p = V_L V_W (A_{max} + V_H) \tag{33}$$

where A_{max} is the maximum vibrating amplitude of the corresponding design. For the case where the coil vibrates higher than the magnets, the amplitude was recorded at $u = L + 47.00$mm, which corresponds to the maximum length of the coil. Under the same base acceleration, the power density is

$$P_D = \frac{P_L^{max}}{V_p} \tag{34}$$

where P_L^{max} is the maximum peak power output at the load resistance. Table 4 tabulates the power density parameters for all designs. ω_{max} in Table 4 refers to the frequency corresponding to P_L^{max}. Fig. 20 displays the peak power output and power density comparison between all three designs for all three cases.The results in Fig. 20 shows that the 2DOF design for Case 1 recorded the highest overall P_D, but also the largest V_p due to its high vibration amplitude. However, the P_D for Cases 2 and 3 in the 2DOF design is lower than the corresponding SDOF and 2SDOF design. Additionally, an increasing trend in P_L^{max} can be observed at the first mode freqeuncy of the 2DOF design as the mass added increases from Case 3 to Case 1. This is due to the fact that the first mode response of a 2DOF system is proportional to the un-coupled frequency ratio of Mass 1 and Mass 2 (ω_r) as shown

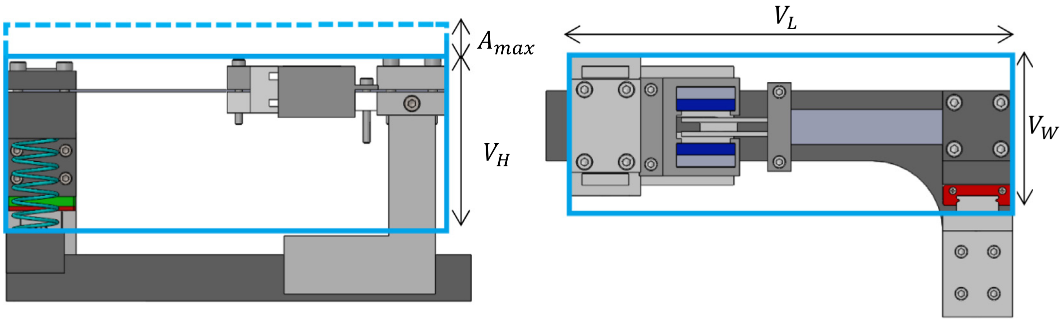

Fig. 19. Volume of the harvester for all designs under non-vibrating condition.

Table 4
Optimum load resistance, peak power output, practical volume and power density for each tested designs.

Design	Case	ω_{max} (Hz)	R_L^{opt} (Ω)	P_L^{max} ($\times 10^{-3}$ W)	V_p ($\times 10^{-4}$ m^3)	P_D (Wm^{-3})
SDOF	1	13.4	15.1	15.6	10.51	14.8
	2	18.9	22.2	16.0	10.31	15.5
	3	29.2	53.2	10.3	10.08	10.2
2SDOF	1	13.3	15.2	15.0	10.51	14.3
	2	18.9	22.2	15.9	10.31	15.4
	3	29.2	53.2	10.3	10.33	9.97
2DOF	1	9.5	8.9	27.7	11.64	23.8
	2	11.4	7.5	12.5	10.67	11.7
	3	13.5	6.8	4.7	10.05	4.7

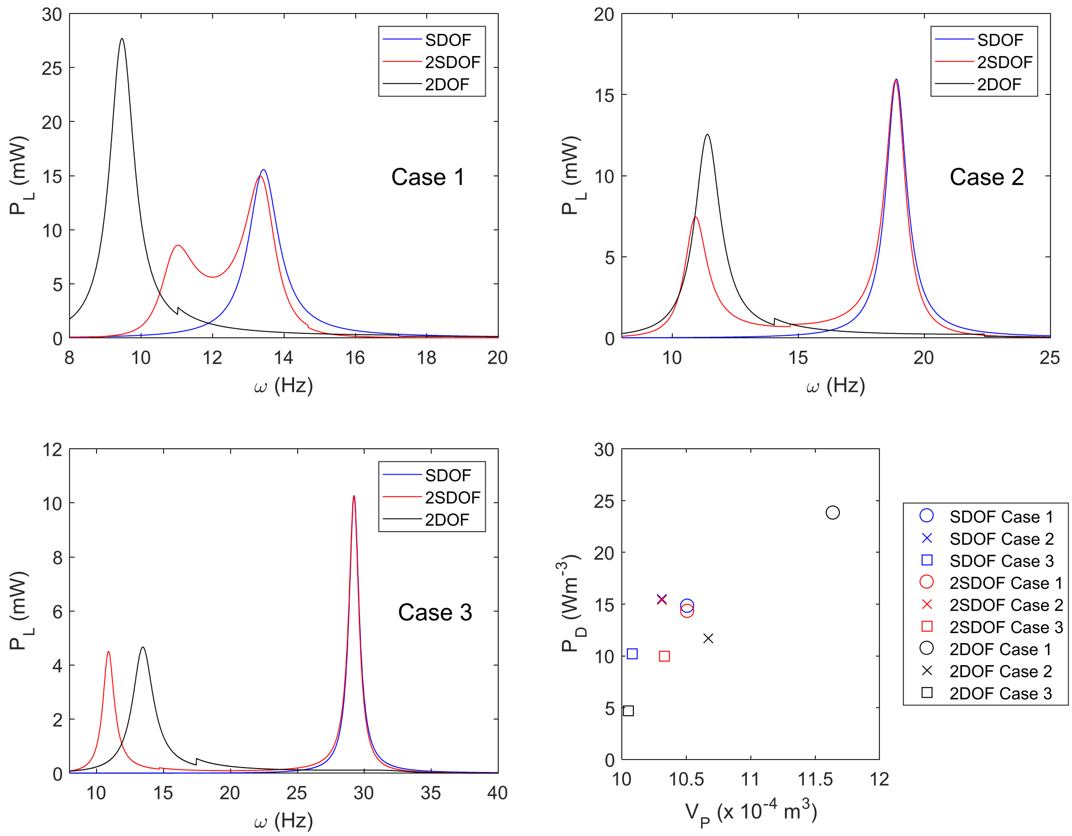

Fig. 20. Power output and power density comparison between all designs for Cases 1, 2 and 3.

$$\omega_r = \frac{\omega_1}{\omega_2} = \sqrt{\frac{k_1 m_2}{k_2 m_1}} \tag{35}$$

where k_1, k_2, m_1 and m_2 are parameters described in Fig. 1. Increasing ω_r would increase the first mode response of the system, but would also reduce the second mode response. Nevertheless, this suggests that under the condition where ω_r is high, the 2DOF design would be superior to the SDOF and 2SDOF design in terms of power density. The P_L^{max} and P_D of the 2SDOF design is very similar to the SDOF design. However, the 2SDOF design is observed to have two operational natural freqeuncies corresponding to the coil and the magnets. In addition, the power output generated between the two natural freqeuncies are larger than the SDOF design, becoming more significant when the two natural freqeuncies are closer to each other as observed in Case 1, hence improving its operational bandwidth.

The mass of the added mass on the coil cantilever beam was then increased in the analytical analysis to match the natural frequency of the SDOF and 2SDOF design with the 2DOF design. It was not possible to analytically compare the 2DOF design beyond 13.5 Hz, as that would require a change in the spring constant value, k_1 (for the sake of maintaining the same volume), in where the new spring damping, c_1, would then be unknown. However, the damping for the cantilever beam in the SDOF and 2SDOF design can be predicted using Eq. (27). Fig. 21 illustrates the comparison for P_L^{max}, P_D and V_p for all three designs.

Fig. 21 shows that P_L^{max} decreases with ω_{max} for the SDOF design. However, the amplitude of the SDOF design can be seen to increase with decreasing ω_{max}, as implied by the increase in V_p. This contradicts the common belief in where the maximum power output of a vibration energy harvester increases with decreasing natural frequency when under a constant base acceleration input. The reason for this is due to the large damping at lower frequencies, leading to a decrease in output voltage. A similar observation was made by Foong et al. [30], suggesting the existence of an optimum natural frequency for different harvesters. The magnitude of P_L^{max} and P_D for the 2SDOF design is shown to be slightly lower than the SDOF design. In addition, a sudden drop in P_L^{max} and P_D is observed when the natural frequency of the coil cantilever beam approaches the natural frequency of the magnets (10.89 Hz). The reason for this is due to the decrease in phase difference $(\theta_c - \theta_m)$ between the two vibrating components, reaching a zero phase difference when their natural frequencies are equal. Based on Eq. (25), this would lead to a decrease in X_r and hence the maximum power output of the design. This suggests that while bringing the natural frequencies of the coil and the magnet closer can improve the design's bandwidth, it can also deteriorate its power

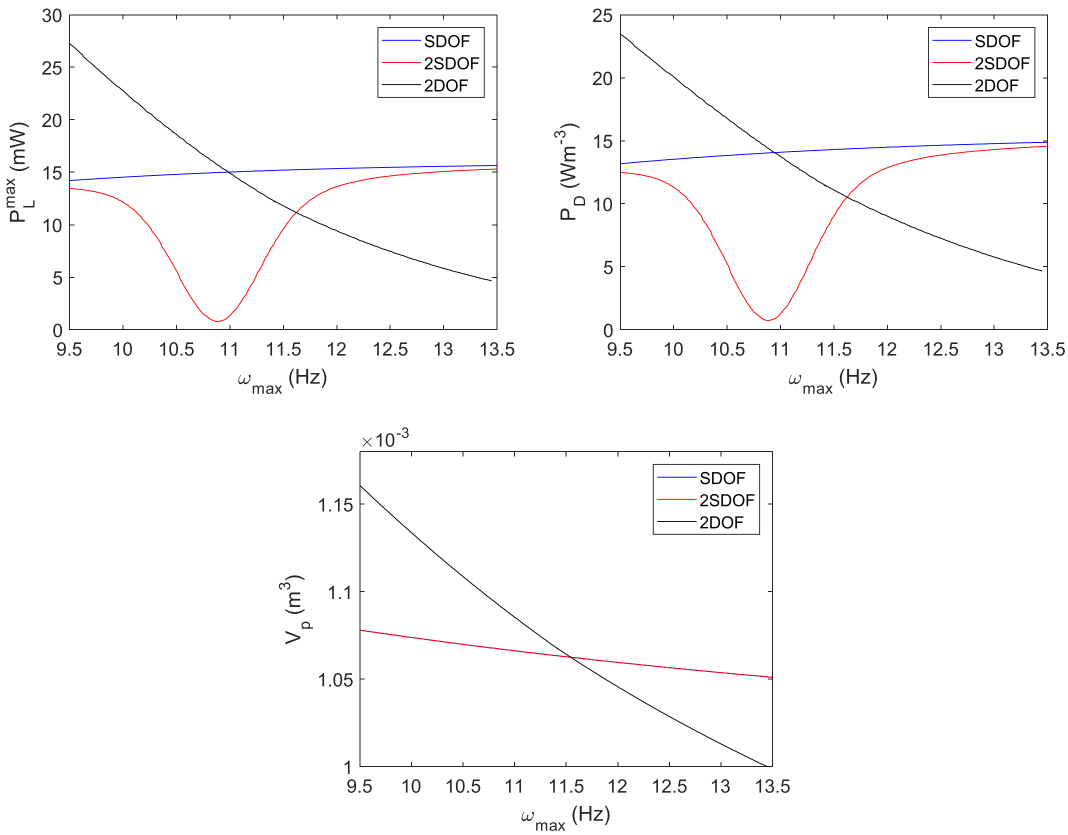

Fig. 21. Power output, power density and volume comparison between all designs under optimum load resistance for a natural frequency range between 9.5 Hz and 13.5 Hz.

output. It is worth to mention that if the difference in natural frequencies between the coil and the magnets are relatively large, the 2SDOF design would produce the same P_L^{max} as the SDOF design as seen in Table 4 for Case 3. Nevertheless, under the same condition, the 2SDOF design would also have two operational natural frequencies. Contrary to the SDOF and 2SDOF designs, the P_L^{max} and P_D of the 2DOF design was seen to increase when ω_{max} decreases. It is shown that under the current setup, the 2DOF design would perform better than the SDOF and 2SDOF design when ω_{max} is approximately lower than 11 Hz, despite the increase in amplitude and V_p. At 9.5 Hz, the P_D of the 2DOF design was recorded to be 78.1% higher than the SDOF design. This difference is expected to increase at natural frequencies below 9.5 Hz.

7. Conclusion

In this study, the use of a spring to amplify the performance of a conventional SDOF cantilever beam-based electromagnetic vibration energy harvester was analysed. The effect of a dynamic friction surface on the voltage output of the harvester was also studied. A spring was introduced to modify the conventional SDOF design into a 2SDOF system and a 2DOF system. The governing equations for these two systems and a base-excited cantilever beam were derived. In addition, a friction model for the case of a dynamic friction surface was developed, with two different theories assumed on how the friction force changes at the isolation frequencies. An experiment was conducted to analyse the output response of the modified designs for three different cases, with each case representing a different natural frequency for the designs. In addition, a FEA analysis was also performed for the same scenarios. The theoretical results displayed a good agreement with the FEA simulation and the experimental results for all three cases. However, it was found that the finite element analysis agreed more with the Theory 1 which corresponded to the modified Coulomb friction model. On the other hand, experimental results agreed with the assumption made in Theory 2, which is the classical Coulomb friction model. The analysis also suggests that the SDOF system would not experience the stick condition when subjected to a dynamic friction surface. Further analysis showed that it was possible to tune the friction force to achieve a more significant voltage peak at the isolation frequencies. This would not be possible if a static friction surface was considered instead. Finally, the power output and the power density of all three designs were compared. It was found that below a certain natural frequency, the 2DOF design proved to be better than the conventional SDOF and 2SDOF design in terms of maximum peak power output and power density. The 2SDOF and SDOF design displayed a very similar power density for all tested cases. Nevertheless, the 2SDOF design displayed two different frequency ranges where significant power can be produced and an improved power output in the region between these two frequency peaks, resulting in an enhanced frequency bandwidth when the two natural frequencies are relatively closer to each other. However, if the two natural frequencies are too close to each other, the power output of the 2SDOF design would significantly drop. Overall, the 2DOF design has the potential to maximise the power output of the harvester. On the other hand, while the power output of the 2SDOF design cannot be larger than the conventional SDOF design, it can be tuned to have a larger frequency bandwidth. Further work includes optimising the 2DOF design to further improve its performance.

Acknowledgement

The authors would like to acknowledge the funding body from the Taiwan Fellowship program, Ministry of Foreign Affair in Taiwan, the partial support from National Taiwan University, Taiwan and Ministry of Science and Technology under Grant Nos 105-2923-E-002-006-MY3 and 105-2221-E-002-028-MY3 and the Fundamental Research Grant Scheme (FRGS) from Ministry of Higher Education (MOHE) Malaysia, Grant No: FRGS/1/2016/TK03/HWUM/03/1, for funding this research.

References

[1] C.B. Williams, R.B. Yates, Analysis of a micro-electric generator for microsystems, Sens Actuat. A: Phys. 52 (1996) 8–11.
[2] N. Aboulfotoh, J. Twiefel, On developing an optimal design procedure for a bimorph piezoelectric cantilever energy harvester under a predefined volume, Mech. Syst. Signal Process. 106 (2018) 1–12.
[3] C.K. Thein, J.S. Liu, Numerical modeling of shape and topology optimisation of a piezoelectric cantilever beam in an energy-harvesting sensor, Eng. Comput. 33 (2017) 137–148.
[4] V.R. Challa, M.G. Prasad, F.T. Fisher, A coupled piezoelectric–electromagnetic energy harvesting technique for achieving increased power output through damping matching, Smart Mater. Struct. 18 (2009) 095029.
[5] A. Erturk, D.J. Inman, On mechanical modeling of cantilevered piezoelectric vibration energy harvesters, J. Intell. Mater. Syst. Struct. 19 (2008) 1311–1325.
[6] M. Salauddin, M.A. Halim, J.Y. Park, A magnetic-spring-based, low-frequency vibration energy harvester comprising a dual Halbach array, Smart Mater. Struct. 25 (2016) 095017.
[7] C. Wang, Q. Zhang, W. Wang, Wideband quin-stable energy harvesting via combined nonlinearity, AIP Adv. 7 (2017) 045314.
[8] C.M. Saravia, A formulation for modeling levitation based vibration energy harvesters undergoing finite motion, Mech. Syst. Signal Process. 117 (2019) 862–878.
[9] C.K. Thein, F.M. Foong, B.L. Ooi, Effect of repulsive magnetic poles on the natural frequency and the bandwidth of a vibration energy harvester, J. Phys.: Conf. Ser. 1123 (2018) 012019.
[10] C. Lan, W. Qin, Enhancing ability of harvesting energy from random vibration by decreasing the potential barrier of bistable harvester, Mech. Syst. Signal Process. 85 (2017) 71–81.
[11] B.L. Ooi, J.M. Gilbert, Design of wideband vibration-based electromagnetic generator by means of dual-resonator, Sens. Actuat. A: Phys. 213 (2014) 9–18.

[12] F.M. Foong, C.K. Thein, B.L. Ooi, D. Yurchenko, Increased power output of an electromagnetic vibration energy harvester through anti-phase resonance, Mech. Syst. Signal Process. 116 (2019) 129–145.
[13] Z.J. Wong, J. Yan, K. Soga, A.A. Seshia, Multi-degree-of-freedom electrostatic MEMS power harvester, PowerMEMS (2009), Washington DC, USA.
[14] J.Q. Liu, H.B. Fang, Z.Y. Xu, X.H. Mao, X.C. Shen, D. Chen, H. Liao, B.C. Cai, A MEMS-based piezoelectric power generator array for vibration energy harvesting, Microelectronics J. 39 (2008) 802–806.
[15] P.H. Wu, Y.J. Chen, B.Y. Li, Y.C. Shu, Wideband energy harvesting based on mixed connection of piezoelectric oscillators, Smart Mater. Struct. 26 (2017) 094005.
[16] I.C. Lien, Y.C. Shu, Array of piezoelectric energy harvesting by equivalent impedance approach, Smart Mater. Struct. 21 (2012) 082001.
[17] D. Liu, Y. Wu, Y. Xu, J. Li, Stochastic response of bistable vibration energy harvesting system subject to filtered Gaussian white noise, Mech. Syst. Signal Process. 130 (2019) 201–212.
[18] H. Zhua, Y. Lia, W. Shen, S. Zhu, Mechanical and energy-harvesting model for electromagnetic inertial mass dampers, Mech. Syst. Signal Process. 120 (2019) 203–220.
[19] P.L. Green, K. Worden, N.D. Sims, On the identification and modelling of friction in a randomly excited energy harvester, J. Sound Vib. 332 (2013) 4696–4708.
[20] A. Harouna, I. Yamadac, S. Warisawa, Study of electromagnetic vibration energy harvesting with free/impact motion for low frequency operation, J. Sound Vib. 349 (2015) 389–402.
[21] G.C.K. Yeh, Forced vibrations of a two-degree-of-freedom system with combined coulomb and viscous damping, J. Acoust. Society America 39 (14) (1966), https://doi.org/10.1121/1.1909863.
[22] J.P.D. Hartog LXXIII,, Forced vibrations with combined viscous and coulomb damping, London Edinburgh Dublin Phil, Mag. J. Sci. 9 (59) (1930) 801–817.
[23] M. Ranjbar, A. Tadayon, Vibration analysis of multi degree of freedom self excited systems, J. Robotic Mech. Syst. 2 (1) (2017) 1–8.
[24] K. Popp, M. Rudolph, Vibration control to avoid stick-slip motion, J. Vib. Control 10 (2004) 1585–1600.
[25] Y.F. Liu, J. Li, Z.M. Zhang, X.H. Hu, W.J. Zhang, Experimental comparison of five friction models on the same test-bed of the micro stick-slip motion system, Mech. Sci. 6 (2015) 15–28.
[26] W. Sun, Y. Liu, H. Li, D. Pan, Determination of the response distributions of cantilever beam under sinusoidal base excitation, J. Phys.: Conf. Ser. 448 (2013) 012010.
[27] M. Kim, M. Hoegen, J. Dugundji, B.L. Wardle, Modeling and experimental verification of proof mass effects on vibration energy harvester performance, Smart Mater. Struct. 19 (2010) 045023.
[28] B.A.M. Owens, P.M. Brian, Linear and nonlinear electromagnetic coupling models in vibration-based energy harvesting, J. Sound Vib. 331 (2012) 922–937.
[29] Y. Tan, Y. Dong, X. Wang, Review of MEMS Electromagnetic Vibration Energy Harvester, J. Microelectromech. Syst. 26 (1) (2017) 1–15.
[30] F.M. Foong, C.K. Thein, B.L. Ooi, D. Yurchenko, On mechanical damping of cantilever beam-based electromagnetic resonators, Mech. Syst. Signal Process. 119 (2019) 120–137.
[31] C.K. Thein, F.M. Foong, Yi-Chung Shu, Damping ratio and power output prediction of an electromagnetic energy harvester designed through finite element analysis, Sens. Actuat. A: Phys. 286 (2019) 220–231.
[32] M. El-hami, P. Glynne-Jones, N.M. White, M. Hill, S.P. Beeby, E. James, A.D. Brown, J.N. Ross, Design and fabrication of a new vibration-based electromechanical power generator, Sens. Actuat. A: Phys. 92 (2001) 335–342.
[33] Y.C. Shu, I.C. Lien, Efficiency of Energy Conversion for a Piezoelectric Power Harvesting System, J. Micromech. Microeng. 16 (2006) 2429–2438.
[34] Y.C. Shu, I.C. Lien, Analysis of Power Output for Piezoelectric Energy Harvesting Systems, Smart Mater. Struct. 15 (2006) 1499–1512.
[35] HIWIN Technologies Corp., Linear guideway technical information, (2018), retrieved from https://www.hiwin.com/pdf/linear_guideways.pdf.
[36] S. Adhikari, Structural Dynamic Analysis with Generalized Damping Models: Analysis, John Wiley & Sons, 2013.
[37] Dassault Systemes Simulia, What's New in Abaqus 2018, (2018), retrieved from https://www.3ds.com/products-services/simulia/products/abaqus/latest-release/.
[38] C.K. Thein, B.L. Ooi, J.S. Liu, J.M. Gilbert, Modelling and optimization of a bimorph piezoelectric cantilever beam in an energy harvesting application, J. Eng. Sci. Tech. 11 (2) (2016) 212–227.
[39] W.C. Tai, L. Zuo, On optimization of energy harvesting from base-excited vibration, J. Sound Vib. 411 (2017) 47–59.
[40] Y. Liao, H. Sodano, Optimal power, power limit and damping of vibration based piezoelectric power harvesters, Smart Mater. Struct. 27 (2018) 075057.
[41] S.P. Beeby, R.N. Torah, M.J. Tudor, P. Glynne-Jones, T. O'Donnell, C.R. Saha, S. Roy, A micro electromagnetic generator for vibration energy harvesting, J. Micromech. Microeng. 17 (2007) 1257–1265.